Journal of Materials Chemistry A

Novel Self-Assembling Approach for Synthesizing Nanofiber Aerogel Supported Platinum Single Atoms

Journal:	*Journal of Materials Chemistry A*
Manuscript ID	TA-ART-03-2020-003207.R1
Article Type:	Paper
Date Submitted by the Author:	01-Jul-2020
Complete List of Authors:	Zhang, Haojie ; Donghua University, College of Materials Science and Engineering, Zhao, Yonghui; Shanghai Advanced Research Institute, Sun, Yu; Hokkaido University Institute for the Advancement of Higher Education, Xu, Qing; Shanghai Advanced Research Institute Yang, Ruoou; Chinese Academy of Sciences, Shanghai Institute of Applied Physics Zhang, Hao; Shanghai Institute of Applied Physics, Lin, Chao; Donghua University, College of Materials Science and Engineering Kato, Kenichi; JARSI/SPring-8, Li, Xiaopeng; Donghua University, College of Materials Science and Engineering Yamauchi, Miho; Kyushu University, I2CNER Jiang, Zheng; Chinese Academy of Sciences, Shanghai Institute of Applied Physics

ARTICLE

Novel Self-Assembling Approach for Synthesizing Nanofiber Aerogel Supported Platinum Single Atoms

Received 00th January 20xx,
Accepted 00th January 20xx

DOI: 10.1039/x0xx00000x

Haojie Zhang,[a,†] Yonghui Zhao,[b,†] Yu Sun,[c] Qing Xu,[b] Ruoou Yang,[d] Hao Zhang,[d] Chao Lin,[a] Kenichi Kato,[e] Xiaopeng Li,[a,*] Miho Yamauchi[f,g,*] and Zheng Jiang[d,h,*]

A grand challenge for catalysts engineering is precisely assembling and positioning nanoscale active metals at desired locations while constructing robust functional architectures. This article presents a novel approach for constructing macroscopic Ag-doped manganese oxide aerogels (up to 2 L) while homogeneously incorporating active Pt single atoms (Pt/Ag-MnO_2) based on a solution-solid-solid (SSS) mechanism. AgO_x seeds were identified as key species for triggering the octopus-like growth of MnO_2 nanofibers and inserting Ag and Pt into the MnO_2 crystalline framework. The interconnection and entanglement among nanofibers allowed the formation of mechanically strengthened hierarchical structures, leading to one of the most robust manganese-based aerogels to date. Impressively, the Pt/Ag-MnO_2 aerogel also possessed promising selectivity and stability toward the electrocatalytic oxygen reduction reaction, with Pt showing a high mass activity of 1.6 A/(mg_{Pt}) at 0.9 V vs. RHE. Experimental characterization and theoretical calculation confirmed Pt single atoms to be located at substitutional lattice sites, which reduce the overall oxygen reduction barriers. Our approach suggests that SSS or other analogous nanofiber or nanowire growth strategy is powerful in controlling structural formation over the entire range of length scales while being applicable to fabricate single-atom catalysts.

Introduction

Aerogels are an extreme class of porous materials having ultralow stacked densities (ρ, ranging from 0.8 to 0.001 g/cm^3), and porosities larger than 80%.[1-3] Aerogels can effectively preserve the unique physical-chemical properties of their nanoscale functional units while retaining them in a single and effectively interconnected macroscopic body.[4] Aerogels possess a continuous hierarchical pore structure, which facilitates mass transport throughout the three-dimensional (3D) architecture with nearly no 'dead' region. These structural features make aerogels as ideal supports for the preparation of energy conversion and storage devices and heterogeneous catalysis applications. To date, various inorganic aerogels such as silica,[5] carbon materials (e.g., graphene and carbon nanotubes),[6, 7] metals (e.g., Au, Pd, and Pt)[8] and metal chalcogenides (e.g., CdS, CdTe, and PbS)[9] have been synthesized. Among them, 3D transition metal oxide aerogels are of technological importance because of their abundance and extensive applications as electrode materials, catalysts or catalytic supports.[10-12] However, the organization of nanocrystalline metal oxide units into a 3D architecture still remains challenging while using self-assembly to achieve desired macroscale properties.[13, 14] For example, most of the transition metal-based aerogels synthesized to date are fragile and require laborious supercritical drying techniques. The addition of a cross-linker or template can improve the mechanical strength of the aerogel at the expense of decreasing the specific activity per volume (or mass).[15] Therefore, the development of a novel fabrication method following the one-pot macroscopic assembly of metal oxide aerogels with improved physical-chemical properties is highly desirable.

Single-atom catalysts (SACs) have recently attracted tremendous interest owing to their reduced material costs and intriguing physical-chemical properties including low coordination environment, quantum-size effect, and strong electronic metal-support interaction (EMSI), thereby enhancing their catalytic performance.[16-31] To date, various methodologies such as impregnation, co-precipitation, atomic layer deposition and pyrolysis of metal-organic frameworks have been

[a] State Key Laboratory for Modification of Chemical Fibers and Polymer Materials & College of Materials Science and Engineering, Donghua University, No. 2999 North Renmin Road, Songjiang District, Shanghai 201620, China
[b] CAS Key Laboratory of Low-Carbon Conversion Science and Engineering, Shanghai Advanced Research Institute (SARI), Chinese Academy of Sciences (CAS), No. 100, Haike Road, Pudong New District, Shanghai 201210, China
[c] Institute for the Advancement of Higher Education, Hokkaido University, North-10 West-8 Kita-ku, Sapporo 060-0817, Japan
[d] Shanghai Synchrotron Radiation Facility, Zhangjiang Lab, Shanghai Advanced Research Institute (SARI), Chinese Academy of Sciences (CAS), No. 239 Zhangheng Road, Pudong New District, Shanghai 201203, China
[e] RIKEN SPring-8 Center, 1-1-1 Kouto, Sayo-cho, Sayo-gun, Hyogo 679-5148, Japan
[f] International Institute for Carbon-Neutral Energy Research (WPI-I^{2}CNER), Kyushu University, Motooka 744, Nishi-ku, Fukuoka 819-0395, Japan
[g] Advanced Institute for Materials Research(AIMR), Tohoku University, 2-1-1 Katahira, Aoba-ku, Sendai, 980-8577 Japan
[h] Shanghai Institute of Applied Physics, Chinese Academy of Science, No. 2019 Jia Luo Road, Jiading district, Shanghai 201800, China
† H. Zhang and Y. Zhao contribute equally to this work.
* Coresponding authors: Prof. X. Li (xiaopeng.li@dhu.edu.cn)
Prof. M. Yamauchi (yamauchi@i2cner.kyushu-u.ac.jp)
Prof. Z. Jiang (jiangzheng@sinap.ac.cn)

Electronic Supplementary Information (ESI) available: [details of any supplementary information available should be included here]. See DOI: 10.1039/x0xx00000x

developed.[32-41] However, despite the ultra-fine metal dispersion achieved, SACs face the same issues of conventional supported catalysts. Thus, an inadequate porous structure engineering may lead to the limited exposure of active sites.[42] Moreover, only powdered SACs have been prepared so far,[29, 30, 32-39, 43-46] and these materials need to be assembled into films, pellets, or monoliths for practical applications. Recently, Zhu et al. reported an iron-based single-atom electrocatalyst (SAEC) supported on a carbon aerogel using Te nanowire as a template, which showed excellent electrocatalytic activities.[47] Notably, to the best of our knowledge, SACs supported by metal oxide aerogel have not been reported. This probably can be explained by the difficulty of homogeneously positioning single atoms in a macroscopic 3D material during aerogel formation.

Over the past decades, abundant knowledge has been built on nanowire/nanofiber growth involving well-identified mechanisms such as solution-liquid-solid (SLS), solution-solid-solid (SSS) and vapor-liquid-solid (VLS) growth of doped nanowires or nanofibers.[48-52] Foreign dopants can be homogeneously incorporated into the nanofiber body through a growth catalyst located at the nanofiber tip. Nanofibers have been also proven as ideal components for constructing functional aerogels.[53-57] Based on previous reports, we developed a novel concept of taking advantage of the nanofiber growth mechanism. Nanofiber unit may be self-assembled into the aerogel form, while simultaneously incorporating single atoms of interests into the crystalline framework of nanofibers. We believe that the successful development of this concept will open a new avenue for SAC synthesis while endowing aerogels with enhanced performance and new functionalities.

Here, we demonstrate the first example of applying an SSS mechanism to construct an Ag-doped α-MnO_2 (Ag-MnO_2) nanofiber aerogel with the incorporation of highly active Pt single atoms into the crystalline lattice of MnO_2. AgO_x nanoparticles severed as seeds, triggering an octopus-like growth mode. The as-formed MnO_2 nanofibers were highly entangled and interconnected, thereby providing the self-assembled hierarchical aerogel monolith with outstanding mechanical strength. Interestingly, Pt atoms were firstly incorporated through AgO_x seeds and subsequently into the Ag-MnO_2 crystalline lattice upon continuous axial growth of the nanofiber during the hydrothermal reaction. The presence of homogenously distributed Pt single atoms and lattice doping sites were validated and characterized by synchrotron radiation X-ray diffraction (SRXRD), X-ray absorption spectroscopy (XAS) and abbreviation-corrected high angle annular dark-field scanning transmission electron microscopy (HAADF-STEM). As a proof-of-concept, the as-prepared Pt/Ag-MnO_2 aerogel was employed as an electrocatalyst for oxygen reduction reaction (ORR). Pt/Ag-MnO_2 showed a promising performance with a high Pt mass activity of 1.6 A/(mg_{Pt}) at 0.9 V (vs. RHE). Density functional theory (DFT) calculation unraveled that the presence of Pt single atoms in MnO_2 lowered the overall energy barriers for oxygen reduction reaction, thereby delivering enhanced performance.

Experimental Section

Synthesis of single atoms Pt supported on Ag-MnO_2 aerogel (Pt/Ag-MnO_2)

The single atoms Pt supported on Ag-MnO_2 aerogel was prepared by a hydrothermal reaction of the synthesis of the Ag-MnO_2 aerogel. Typically, $MnSO_4 \cdot H_2O$ (0.005 mol), $(NH_4)_2S_2O_8$ (0.005 mol) and $(NH_4)_2SO_4$ (0.02 mol) were added to the 25 mL Teflon vessel with 17.5 mL DI water, forming a clear solution. Subsequently, a certain amount of $AgNO_3$ and $Pt(NO_3)_2$, determined by the nominal loading of 10 wt% Ag and 1 wt% Pt, were added to the solution with vigorously stirring for 15 min. Then, the Teflon vessel was sealed and transferred into the oven at 140 °C for 12 h. After cooling down to the room temperature, the obtained hydrogel was washed with a large quantity of water. Afterward, the hydrogel was placed in a refrigerator at -70 °C and then freeze-dried for 48 h for obtaining aerogel. Control samples including Ag-MnO_2 and un-doped MnO_2 were prepared in an identical way by controlling the addition of $AgNO_3$ and $Pt(NO_3)_2$.

Material characterization

XRD was carried out on an Ultima IV X-ray diffractometer with Cu Kα radiation (λ=0.15418 nm, Rigaku, Japan). The N_2 adsorption/desorption isotherms were measured by a surface area and porosity analyzer (Tristar II, Micromeritics). The samples were degassed at 120 °C for 6 h under vacuum before analysis. XPS measurements were taken out by using a photoelectron spectrometer (Thermo Fisher Scientific, USA). Calibration of binding energy was carried out by setting the binding energy of C1s peak to 284.8 eV. The morphologies of the as-synthesized samples were examined by a field-emission SEM with the EDS (Oxford, UK). TEM and STEM were used to further confirm the detailed nanostructures (FEI Tecnai G2, USA), and EDS was used to determine the Ag and Pt loading (Oxford, UK). HAADF-STEM was used to further confirm the Atomic arrangement in the Ag-MnO_2 nanofiber (JEOL-2010, Japan). The mechanical properties were measured by a 5960 Dual Column Tabletop Testing Systems (INSTRON 5967, USA). SRXRD was conducted using radiation (λ=0.80072(4) Å) at RIKEN BL44B2 beamline. X-ray absorption spectroscopy (XAS) measurements were performed at the BL14W1 beamline at the Shanghai Synchrotron Radiation Facility, Shanghai Institute of Applied Physics, China. The electron storage ring operated at 3.5 GeV, equipped with a double Si (111) crystal monochromator.[58] X-ray absorption data was obtained at fluorescence mode and data analysis was performed using the IFEFFIT software package. The amount of the Pt was measured by a Varian 720-ES inductively coupled plasma optical emission spectrometry (ICP-OES).

Electrochemical measurements

Electrocatalytic measurements were performed with a PARSTAT 4000 electrochemistry workstation (Princeton Applied Research, USA) at room temperature using Pt wire and Ag/AgCl

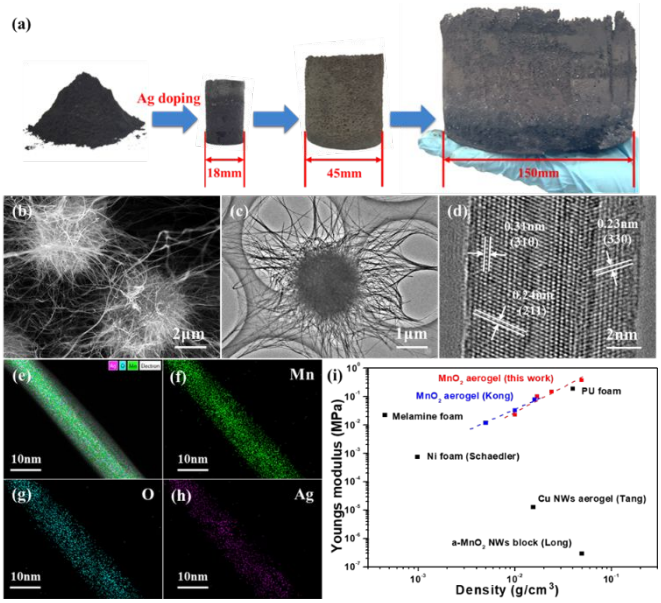

Fig. 1. Characterization of Ag-MnO_2 aerogel. (a) Optical photograph of the un-doped α-MnO_2 nanowire powder and the Ag-MnO_2 aerogels with different sizes. (b) HRSEM, (c) TEM and (d) HRTEM images of the as-prepared Ag-MnO_2 aerogel. (e) the overlay of the distribution of the elements along with an Ag-MnO_2 nanofiber acquired by EDS mapping measurement and the corresponding spectra for individual elements: (f) Mn, (g) O and (h) Ag. (g) Relationship between E and ρ for the Ag-MnO_2 aerogels, together with data from some reported foams/aerogels for comparison. Carbon material aerogels were not included.

(Metrohm, 3M KCl) as counter and reference electrodes. The ORR performance was evaluated on RDE and RRDE setup.

Details of DFT calculation and ORR measurements are provided in the supporting information.

Results and discussion

Synthesis and characterization of robust Pt/Ag-MnO_2 aerogel

Firstly, Ag-MnO_2 aerogel was synthesized in an aqueous solution containing $AgNO_3$, $MnSO_4$, $(NH_4)_2SO_4$, and $(NH_4)_2S_2O_8$ (see details in experimental section). After being vigorously stirred for 1 min, the mixed solution was transferred to a Teflon vessel and subsequently heated in an oven at 140 °C for 12 h. The obtained Ag-MnO_2 hydrogel was freeze-dried to produce a solid aerogel. At the macroscopic scale, Ag-MnO_2 aerogel inherited the shapes of their cylindrical vessels. As shown in Fig. 1(a), Ag-MnO_2 aerogel were successfully prepared with a diameter of up to 15 cm with the total volumes of approximately ~ 2 L and the mass of ~ 99.6 g. The preparation of Ag-MnO_2 aerogel can be consistently and cost-effectively scaled-up by simply increasing the size of the vessel used for the hydrothermal processing. The ρ of an Ag-MnO_2 aerogel can be controlled from ~ 10 to ~ 50 mg/cm^3 by linearly increasing the precursor concentration. In contrast, a hydrogel/aerogel could not be produced in the absence of $AgNO_3$, with the average length of the as-grown α-MnO_2 nanofibers was approximately 600 nm (Fig. S1), because these low aspect ratio α-MnO_2 nanofibers did not satisfy the basic conditions for gel formation.[54] The SRXRD pattern for Ag-MnO_2 aerogels (Fig. S2) could be ascribed to a pure α-MnO_2 phase (JCPDS No. 044-0141) with the tetragonal, I4/m, symmetry space group.[59-61]

Scanning electron microscopy (SEM) and transmission electron microscopy (TEM) were used to image microscale morphological features of the as-prepared Ag-MnO_2 aerogel. Low-resolution SEM (LRSEM) images (Fig. S3(a-b)) confirmed the presence of large pores (> 50 μm), which were created by ice crystals, and revealed the solid 3D skeleton of the Ag-MnO_2 aerogel. High-resolution SEM (HRSEM) images (Fig. 1(b) and Fig. S3(c-f)) revealed the aerogel skeleton was composed of spherical cellular structures with the diameters of ~2 μm. TEM images as shown in Fig. 1(c) and Fig. S4(a-b) presented the morphology of a single cellular structure and several interconnected spherical cellulars, which are consistent with the SEM observations. The basic architectural elements of the Ag-MnO_2 nanofibers had an average diameter of ~10 nm (Fig. 1(d) and Fig. S4(c-d)). The Ag-MnO_2 nanofibers were highly entangled and interconnected. These bonded contacts were believed to be crucial for the formation of Ag-MnO_2 aerogel with enough mechanical robustness to survive from handling and freeze-drying. Energy dispersive spectrometry (EDS) mapping revealed that Ag was homogenously distributed in the bodies of the MnO_2 nanofibers (Fig. 1(e-h)). Ag content was determined to be ~ 7.6 wt% by EDS, slightly lower than the theoretical doping amount of 10 wt%. The pore size distribution of Ag-MnO_2 aerogel confirmed the presence of hierarchical pores with the size continuously spanning from 5 to 110 nm (Fig. S5). Fig. 1(i) shows a plot of the compressive Young's modulus

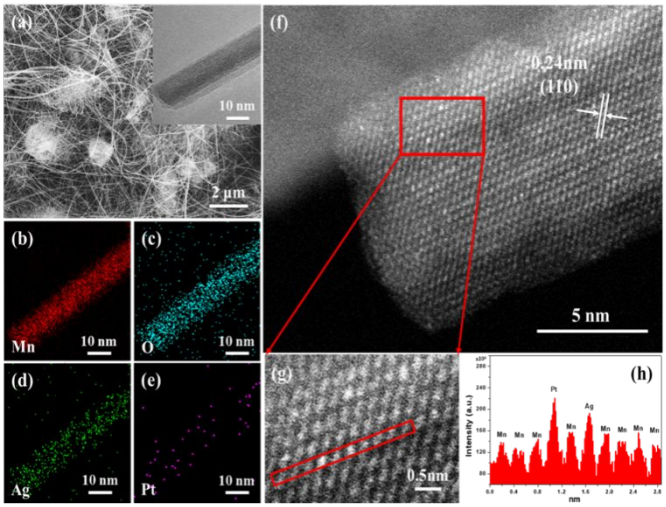

Fig. 2. Electron microscopy characterizations of Pt/Ag-MnO_2. (a) SEM image of the Pt/Ag-MnO_2 aerogel and TEM image (inset) of the single Pt/Ag-MnO_2 nanofiber. EDS element mapping of Pt/Ag-MnO_2 (b) Mn, (c) O, (d) Ag and (e) Pt. (f) HAADF-STEM image of a single Pt/Ag-MnO_2 nanofiber. (g) a magnified view of the area marked in (f). (h) HAADF intensity profile drawn along the red rectangle marked in (g).

ARTICLE

Table 1. Structural Parameters of PtO_2 and Pt/Ag-MnO_2 derived from quantitative EXAFS curve-fitting using the IFEFFIT software, and DFT calculated structure parameters.

Sample	Shell	CN	R(Å)	ΔE_0 (eV)	$\Delta\sigma^2*10^3$ (Å^2)	R-factor (%)
PtO_2	Pt-O	6.0 ± 0.6	2.12 ± 0.02	9.1 ± 2.4	2.13 ± 1.58	1.3
Pt/Ag-MnO_2	Pt-O	6.0 ± 0.6	2.01 ± 0.02	9.9 ± 1.3	1.28 ± 0.69	2.4
	Pt-Mn-1	1.9 ± 0.1	2.90 ± 0.03	2.4 ± 0.5	3.38 ± 1.76	
	Pt-Mn-2	1.8 ± 0.2	3.04 ± 0.03	2.5 ± 0.5	2.53 ± 0.54	
Pt/MnO_2 (DFT results)	Pt-O	6.0	1.99	--	--	--
	Pt-Mn-1	2.0	2.89	--	--	
	Pt-Mn-2	2.0	3.04	--	--	

Note: Pt L_3-edge EXAFS curves fitting parameters: Δk = 3.0 – 12.5 Å^{-1}, Δr = 1.0 – 2.0 Å. CN, coordination number; R, the distance between absorber and backscatter atoms; ΔE_0, inner potential correction; $\Delta\sigma^2$, Debye-Waller factor to account for both thermal and structural disorders; R-factor (%) indicate the goodness of the fit. The obtained S_0^2 of Pt foil was 0.87 and it was fixed in the subsequent fitting of Pt foil L_3-edge data for the catalyst. CN and bond lengths are corresponding to the structures displayed in Fig. 3d.

(*E*) of the Ag-MnO_2 aerogel, which was derived from the slope of the stress-strain curve plotted against ρ as shown in Fig. S6. The *E* of the Ag-MnO_2 aerogel increased with an increase in ρ such that $E \approx \rho^{1.7}$ and reached 375 kPa at ρ = 49 mg/cm^3. To the best of our knowledge, this Ag-MnO_2 aerogel has a higher *E* (for compression) than any other reported manganese-based aerogels. The enhanced physical properties (e.g., mechanical strength) together with the high surface area and the hierarchical structures make Ag-MnO_2 aerogel as an ideal support for SACs.

The incorporation of Pt into the Ag-MnO_2 (Pt/Ag-MnO_2) aerogel was achieved by simply adding $Pt(NO_3)_2$ to the precursor solution prior to the hydrothermal reaction. SEM and STEM characterization revealed that Pt/Ag-MnO_2 shared nearly identical structure features as the Ag-MnO_2 aerogel (Fig. 2(a) and Fig. S7). EDS elemental mapping showed a uniform Pt distribution similar to that of Ag over the entire MnO_2 cellular structure with no Pt aggregates (Fig. 2(b-e)). The Pt and Ag contents were determined to be 0.42 and 6.30 wt%, respectively, by EDS. The Pt content was determined to be 0.36 wt% by inductively coupled plasma optical emission spectrometry (ICP-OES). To further gain insights into the atomic structure of the Pt/Ag-MnO_2, abbreviation-corrected HAADF-STEM imaging with atomic number-contrast (Z-contrast) was conducted on a single nanofiber. Pt and Ag atoms appeared brighter than Mn atoms in the image (Fig. 2(f) and Fig. S7 (e)), while low atomic-number oxygen atoms were not detected by HAADF. In the enlarged image shown in Fig. 2(g) and the line profile drawn along the bright atomic column in Fig. 2(h), two atoms with higher contrast than the surrounding Mn atoms were observed. Since the HAADF signal is proportional to $Z^{1.7}$, we ascribed those two atoms to Pt and Ag based on a rough estimation of the signal intensity.

EDS and STEM results suggested Pt predominantly existed as single atoms. With the aim to confirm the atomic dispersion of Pt in the entire Pt/Ag-MnO_2 aerogel, and to probe the electronic structure and coordination environment, SRXRD, X-ray photoelectron spectroscopy (XPS), X-ray absorption near-edge spectroscopy (XANES) and extended X-ray absorption fine structure (EXAFS) were performed. The SRXRD pattern of Pt/Ag-MnO_2 (Fig. 3(a)) was assigned to α-MnO_2 reflection with no diffraction peaks corresponding to Pt or PtOx being observed, which excluded the presence of large crystalline Pt particles. Rietveld refinement indicated that the crystalline lattice of the Ag-MnO_2 aerogel expanded upon the incorporation of large atomic radius Pt. Thus, Pt/Ag-MnO_2 showed larger a and b dimension (9.854 Å) as compared to Ag-MnO_2 (9.840 Å), while

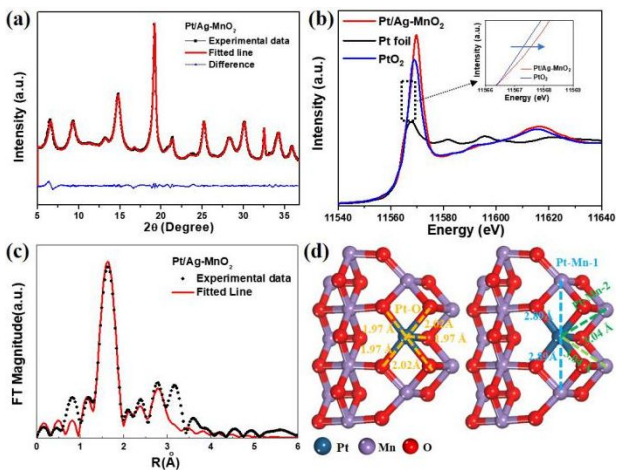

Fig. 3. Structure characterization of Pt/Ag-MnO_2 aerogel by SRXRD, XANES and EXAFS spectroscopy. (a) SRXRD patterns of the Pt/Ag-MnO_2 aerogel. (b) Normalized Pt L_3-edge XANES spectra of the Pt/Ag-MnO_2 aerogel, PtO_2 and Pt foil. The inset picture shows the magnified view of the selected region. (c) The k^3-weighted Fourier transformed EXAFS spectra of the Pt/Ag-MnO_2 aerogel. (d) DFT calculated Pt/MnO_2 structure showing the bond lengths of first shell Pt-O, and high shell Pt-Mn-1 and Pt-Mn-2.

the c dimension remained unchanged (2.858 Å). These results suggested that Pt atoms possibly occupy Mn sites rather than being simply adsorbed at the tunnel or the surface of MnO_2. The profile of the XANES spectra of Pt/Ag-MnO_2 was similar to that of the reference PtO_2 (Fig. 3(b)). However, the intensity of the white and the sharpness of the first intense maxima at ~ ca.11570 eV was higher than that of PtO_2, indicating Pt atoms have a high oxidation state (> +4), which can be ascribed to electron transfer from Pt to the Ag-MnO_2 framework. Fig. 3(c) shows the Fourier transformed EXAFS spectra of the Pt/Ag-MnO_2 aerogel, which included a dominant peak located at ~ 1.6 Å ascribed to the Pt-O contribution with a bond length of 2.01 Å. Two weaker peaks around 2.65 Å were contributed by two types of high shell Pt-Mn coordination (denoted as Pt-Mn-1 and Pt-Mn-2). The EXAFS fitting results are displayed in Table 1. The coordination number (CN) and bond length ($d_{Pt\text{-}Mn\text{-}1}$) for Pt-Mn-1 were estimated to be 1.9 ± 0.1 and 2.90 ± 0.03 Å, respectively. The CN and $d_{Pt\text{-}Mn\text{-}2}$ for Pt-Mn-2 were estimated to be 1.8 ± 0.2 and 3.04 ± 0.03 Å, respectively. No significant contribution from Pt-Pt coordination (~2.8 Å) was observed. We simulated the crystal structure of Pt substituted MnO_2 (Fig. 3(d)). The bond length of first shell Pt-O coordination was determined to be ~1.99 Å. The bond lengths of two types of high shell Pt-Mn coordination including Pt-Mn-1 and Pt-Mn-2 were calculated to be 2.89 Å and 3.04 Å, respectively, which are in good agreement with the EXAFS results as listed in Table 1. Compared with PtO_2 (R = 2.12 ± 0.02 Å), Pt/Ag-MnO_2 aerogel showed a shorter Pt-O bond length (R = 2.01 ± 0.02 Å), thereby suggesting a stronger interaction between Pt and O atoms in Pt/Ag-MnO_2. The above results demonstrated that Pt single atoms were successfully doped into the MnO_2 framework via the substitution of Mn sites.

Identification of aerogel formation and Pt single atoms incorporation mechanism

In order to gain an insight into the aerogel formation and Pt single atoms incorporation mechanism, time-dependent characterization of the reaction intermediates was carried out. During the typical hydrothermal synthesis of un-doped α-MnO_2 nanofibers, the reaction at elevated temperature (>100 °C) is known to process as:[62]

$$Mn^{2+}(l) + S_2O_8^{2-}(l) + 2H_2O(l) \rightarrow MnO_2(s) + 4H^+(l) + 2SO_4^{2-}(l) \quad (1)$$

However, when $AgNO_3$ is added to the precursor solution, this reaction can process rapidly at room temperature (Fig. S8), indicating that the Ag species might effectively catalyze reaction (1). Black precipitates of the mixed precursor solution were collected prior to hydrothermal treatment. According to XRD, SEM, and TEM analyses, a large number of AgO nanoparticles (Fig. 4(a)) and spherical aggregates of short Ag-MnO_2 nanofibers with relatively low crystallinity (Fig. S9) were found to form. Fig. 4(b-g) show results from TEM, XRD, and XPS measurements of the reaction intermediates over time. With an increase in the hydrothermal reaction time (*t*), the crystallinity of the MnO_2 products increased. After 1 h (Fig. 4(c)), spherical MnO_2 cellular structures formed, but these structures formed black precipitates. At *t* = 3 h (Fig. 4(d)), the

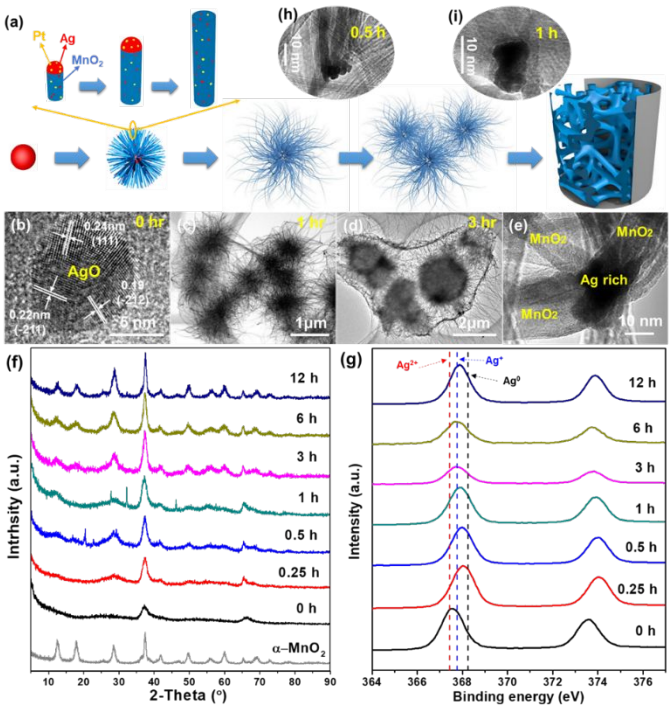

Fig. 4. Doping mechanism of the Pt/Ag-MnO_2 aerogel. (a) Proposed growth mechanism of the Ag-MnO_2 aerogels and Pt/Ag-MnO_2. The red sphere and blue wires represent an AgO_x particle and Ag-MnO_2 nanofibers, respectively. Time-dependent (b-e) TEM, (f) XRD and (g) XPS (Ag 3d) measurements of reaction intermediates during Ag-MnO_2 hydrogel formation. (h-i) TEM image of reaction intermediate collected at 0.5 h (h) and 1 h (i) during the preparation of Pt/Ag-MnO_2 aerogel.

α-MnO_2 nanofibers were longer (> 5 μm), and their secondary structures became entangled and interconnected. A relatively weak hydrogel formed under these conditions. As the hydrothermal reaction proceeded beyond 3 h, the Ag-MnO_2 nanofibers became longer (> 10 μm), and the 3D interconnection (Fig. 4(e), *t* = 12 h) and mechanical strength of the Ag-MnO_2 hydrogel were improved. Interestingly, the tops of several nanofibers were found to be fused together by an AgO_x-based seed, indicating an octopus-like growth mode and the TEM and STEM images of MnO_2 nanofibers sharing Ag catalysts are shown in Fig. S10. EDS elemental analysis confirmed the high Ag content of the growing catalyst (Fig. S11). According to the time-dependent XPS measurements (Fig. 4(g)), AgO was rapidly reduced on the nanofibers surface, because of its thermodynamic instability. The chemical valence of Ag was between Ag^+ and Ag^0 during the first 0.5 h, but Ag^+ was the primary species present during the MnO_2 hydrogel formation process (*t* ≤ 12 h). AgO_x nanoparticles are believed to strongly catalyze and promote the growth of α-MnO_2 nanofibers such as those shown in Fig. 4(a) via a SSS mechanism. The growth reactions for this process might be as below

$$S_2O_8^{2-}(l) + Ag_2O(s) + H_2O(l) \rightarrow 2AgO(s) + 2H^+(l) + 2SO_4^{2-}(l) \quad (2)$$

$$H_2O(l) + 2AgO(s) + Mn^{2+}(l) \rightarrow MnO_2(s) + 2H^+(l) + Ag_2O(s) \quad (3)$$

With growth kinetics enhanced by the AgO_x seeds at one end of the MnO_2 nanofibers, MnO_2 nanofibers underwent rapid axial growth near the AgO_x rather than radial growth. The longer nanofibers facilitated more elaborate entanglement. Moreover, several MnO_2 nanofibers could share a single AgO_x nanoparticle catalyst such that the AgO_x nanoparticles not only catalyzed

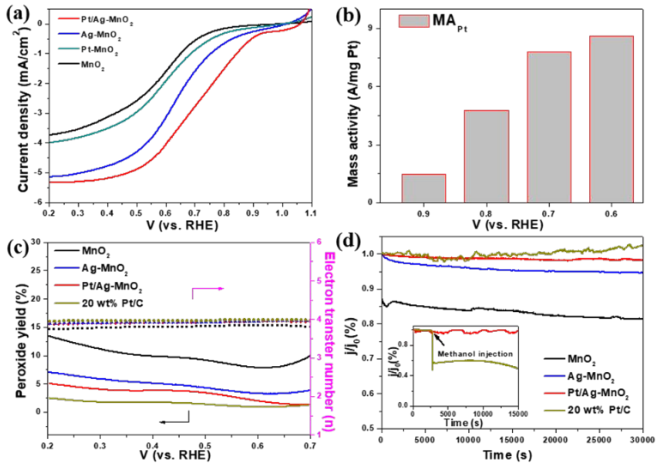

Fig. 5. Electrocatalytic performance evaluation. (a) ORR polarization curves of the Pt/Ag-MnO_2 aerogel, Ag-MnO_2 aerogel, Pt-MnO_2, and undoped α-MnO_2. (b) Calculated MA_{Pt} on different potentials. (c) Dependence of the peroxide yield (left axis) and the electron transfer *n* (right axis) derived from the rotating ring-disk electrode (RRDE) data. (d) Chronoamperometric responses recorded at 1.97 V *vs.* RHE of MnO_2, Ag-MnO_2, Pt/Ag-MnO_2 and 20 wt% Pt/C. The methanol tolerance test is shown inset of (d).

growth but also acted as cross-linkers to fuse nearby nanofibers. The combination of these unique growth features leads to the formation of Ag-MnO_2 aerogel with extraordinary mechanical properties. Beyond its important role as a catalyst for the hydrogel formation, AgO_x catalysts were doped into MnO_2 with the growth of nanofiber due to the high solubility of ionic Ag in MnO_x.[39] Of note, the Ag catalyst-based SSS growth mechanism was different from others reported in the literature. Meng et al.[63] and Li et al.[64] obtained Ag catalyzed MnO_2 nanostructures only in the powder form.

The incorporation of Pt single atoms also strongly depends on the AgO_x catalysts. A control experiment without the addition of $AgNO_3$ was carried out. Only PtO_x aggregates were obtained at the MnO_2 nanofiber surface (Fig. S12). TEM images of reaction intermediates of Pt/Ag-MnO_2 aerogel collected at 0.5 h (Fig. 4(h)) and 1 h (Fig. 4(i)) were similar to those of Ag-MnO_2 aerogel, indicating the addition of Pt ions did not change the SSS nanofiber growth mechanism. The EDS mapping (Fig. S13) confirmed that the presence of AgO_x growth catalysts and Pt distributed at the AgO_x seeds as well as in the nanofibers. Fig. 4(a) shows the schematic of the proposed Pt incorporation mechanism. We hypothesized that Pt was firstly deposited at the AgO_x seeds and then incorporated into the crystalline framework of Ag-MnO_2 with the elongation of nanofibers. As depicted by *ex-situ* XPS characterization, the valence of Ag species was between Ag^+ and Ag^0 during the first 0.5 h. The incorporation of Pt single atoms may firstly proceed with Pt deposition at AgO_x may proceed *via* galvanic displacement between Pt ions and Ag^0, and then followed by spontaneous incorporation into MnO_2.

Electrocatalytic activities of Pt/Ag-MnO_2

The intriguing physical-chemical properties of the Pt/Ag-MnO_2 aerogel inspired us to use it as an electrocatalyst for oxygen reduction reaction (ORR). Fig. 5(a) shows the ORR polarization curves measured at a rotating disk electrode (RDE) in an oxygen-saturated electrolyte (1 M KOH). Ag-MnO_2 aerogel showed a substantial improvement in the ORR activity after incorporation of Pt single atoms. Pt/Ag-MnO_2 aerogel had significantly higher positive onset potential (E_{onset} = 1.05 V vs. RHE, which is defined as the current density reaching 0.1 mA/cm^2), half-wave potential ($E_{1/2}$ = 0.71 V), and larger diffusion-limited current density (J_l = 5.32 mA/cm^2) than that of Ag-MnO_2 aerogel and 10 wt% Pt/C (Fig. S14(a)). Additionally, Pt/Ag-MnO_2 demonstrated a nearly same E_{onset} as 20 wt% Pt/C (Fig. S14(a)). In contrast, Pt/MnO_2 prepared without AgO_x seeds exhibited significantly inferior performance, which was only slightly higher than that of the un-doped α-MnO_2. This stark difference highlights the power of Pt single atoms in promoting ORR. We calculated the Pt mass activity (MA_{Pt}) based on the ORR kinetic current density (j_k) and the ICP-OES data. The MA_{Pt} reached as high as 1.6 A/(mg_{Pt}) at 0.9 V (Fig. 5(b)). RDE voltammograms at different rotating speeds were performed (Fig. S14(b)). Using the Koutechy–Levich equation (K–L), the electron transfer number (*n*) of the Pt/Ag-MnO_2 aerogel was calculated to be ca. 3.92 at 0.6 V (as shown in the inset of Fig S14), indicating a nearly ideal 4-electron pathway. The good linearity of the K–L plot suggested a first-order reaction kinetic. To further verify the reaction pathway and quantitatively monitor the reaction intermediates, rotating ring disk electrode (RRDE) experiments were carried out. Fig. 5(c) shows the dependence of the peroxide yield and *n* on the potential calculated from the disk and ring current. The peroxide yield of the Ag-MnO_2 aerogel was observed to be improved to less than 5% after incorporating Pt single atoms. The *n* on the Pt/Ag-MnO_2 aerogel in the potential range from 0.2 to 0.7 V was nearly constant at around 3.9, agreeing well with the RDE results. Apart from its high ORR activity and selectivity, Pt/Ag-MnO_2 aerogel also exhibited superior stability and resistance against methanol crossover. In a continuous chronoamperometric measurement for 30000 s (Fig. 5(d)), 98.4% of the initial ORR current was retained at the Pt/Ag-MnO_2 aerogel. Ag-MnO_2 retained 94.6% of its initial ORR current under the same conditions. In sharp contrast, undoped α-MnO_2 lost 19% of its initial ORR current in the same period. As demonstrated in the inset of Fig. 5(d), the ORR activity of the Pt/Ag-MnO_2 aerogel was retained with only a 2% loss of current after the addition of methanol through 12600 s of operation. This loss was much smaller than those of 20 wt% Pt/C (44%), suggesting that the superior methanol tolerance of Pt single atoms over metallic Pt nanoparticles in 20 wt% Pt/C.

Understanding the origin of the high activity of Pt single atoms

To explore the possible role of Pt single atoms in promoting the activity of Ag-MnO_2, we investigated the changes in the geometric and electronic effects by the Vienna Ab initio Simulation Package (VASP) code[65-67] based on self-consistent DFT on the MnO_2 (100) surface. In order to obtain deeper

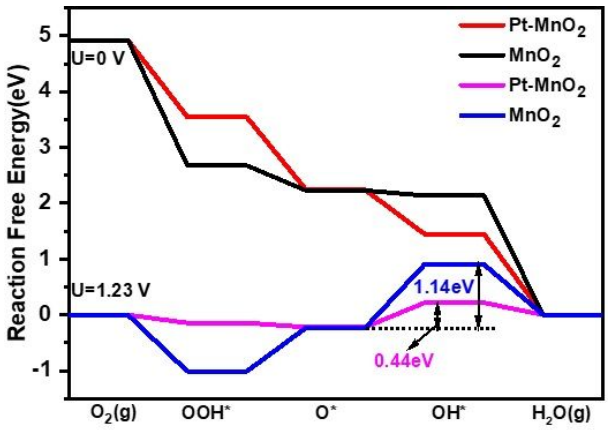

Fig. 6. Energy profiles for oxygen reduction reaction at 0 and 1.23 V (RHE) over different catalytic sites.

insights into the ORR mechanism on MnO_2 and Pt-MnO_2 (Pt substituting Mn site) surfaces, the energy profiles for the reactions taking place at 0 and 1.23 V (*vs.* RHE) over different catalytic sites were obtained with DFT calculations based on the computational hydrogen electrode (CHE) method developed by Nørskov and co-workers (Fig. 6).[68-72] The top view of optimized adsorption configurations of the reaction intermediates, i.e. *OOH, *O, H and *OH, on the surfaces of MnO_2 and Pt-MnO_2 surfaces are shown in Fig. S15. It is obvious that at 1.23 V, OH* protonation to H_2O is the potential RDS over the Pt-MnO_2 surface with a reaction free energy (ΔG) of 0.44 eV. In contrast, *OH protonation to H_2O for MnO_2 surface with ΔG = 1.14 eV for the MnO_2 surface. Such a decrease of reaction free energy well explains the experimentally observed better performance of Pt-MnO_2 for ORR than that of MnO_2, and the Pt-MnO_2 surface has higher ORR activity than MnO_2 surface.

Conclusions

In summary, we identified an SSS mechanism to construct an Ag-MnO_2 aerogel consisting of sophisticated hierarchical structures at the liter scale while simultaneously achieving homogenous incorporation of Pt single atoms. AgO_x nanoparticles acted as catalysts triggering the octopus-like growth of MnO_2. Because of its atomic and microscale structural merits, Pt/Ag-MnO_2 aerogel showed substantial improved physical-chemical properties. Pt/Ag-MnO_2 aerogel exhibited the highest elastic modulus E (for compression) among the reported manganese-based aerogels and possessed high catalytic activity, selectivity and stability towards ORR processes. Impressively, Pt single atoms displayed a high mass activity of 1.6 A/(mg_{Pt}). Together with HAAD-STEM, XPS, SRXRD and EXAFS results suggested the presence of Pt single atoms substituting Mn sites with electron-deficient character due to the strong EMSI. The theoretical calculation also unraveled that the incorporation of Pt single atoms markedly decreased the overall ORR barriers. Our work suggests the great potential of applying SSS mechanism and other analogous growth mechanisms (e.g. VLS and SLS) in synthesizing SACs supported on 3D structures.

Conflicts of interest

There are no conflicts to declare.

Acknowledgments

X. L. acknowledges support from the National Natural Science Foundation of China (No. 21972163), the Fundamental Research Funds for the Central Universities and DHU Distinguished Young Professor Program. Z. Jiang acknowledges financial support from the Joint Fund U1732267. M. Y. thanks the JSPS KAKENHI (No. JP 18H05517) and JST-CREST for financial supports, and Riken SPring-8 for the approval of the SRXRD measurement (20190028). The authors acknowledge the help from Prof. Shuyuan Zhang (USTC) for the HAADF-STEM measurement. XANES and EXAFS studies were carried out at the BL14W1 beamline at Shanghai Synchrotron Radiation Facility (16ssrf00787).

References

1. N. Leventis, N. Chandrasekaran, A. G. Sadekar, S. Mulik and C. Sotiriou-Leventis, *J. Mater. Chem.*, 2010, **20**, 7456-7471.
2. M. Mecklenburg, A. Schuchardt, Y. K. Mishra, S. Kaps, R. Adelung, A. Lotnyk, L. Kienle and K. Schulte, *Adv. Mater.*, 2012, **24**, 3486-3490.
3. M. A. Aegerter, N. Leventis and M. M. Koebel, *Aerogels handbook*, Springer Science & Business Media, LLC, New York, 1 edn., 2011.
4. A. C. Pierre and G. M. Pajonk, *Chem. Rev.*, 2002, **102**, 4243-4265.
5. A. Soleimani Dorcheh and M. H. Abbasi, *J. Mater. Process. Tech.*, 2008, **199**, 10-26.
6. M. B. Bryning, D. E. Milkie, M. F. Islam, L. A. Hough, J. M. Kikkawa and A. G. Yodh, *Adv. Mater.*, 2007, **19**, 661-664.
7. V. Chabot, D. Higgins, A. P. Yu, X. C. Xiao, Z. W. Chen and J. J. Zhang, *Energy Environ. Sci.*, 2014, **7**, 1564-1596.
8. W. Liu, A. K. Herrmann, N. C. Bigall, P. Rodriguez, D. Wen, M. Oezaslan, T. J. Schmidt, N. Gaponik and A. Eychmuller, *Acc. Chem. Res.*, 2015, **48**, 154-162.
9. J. L. Mohanan, I. U. Arachchige and S. L. Brock, *Science*, 2005, **307**, 397-400.
10. H. Dau, C. Limberg, T. Reier, M. Risch, S. Roggan and P. Strasser, *ChemCatChem*, 2010, **2**, 724-761.
11. J. Jiang, Y. Y. Li, J. P. Liu, X. T. Huang, C. Z. Yuan and X. W. Lou, *Adv. Mater.*, 2012, **24**, 5166-5180.
12. S. M. Jung, H. Y. Jung, W. Fang, M. S. Dresselhaus and J. Kong, *Nano Lett.*, 2014, **14**, 1810-1817.
13. D. R. Rolison, J. W. Long, J. C. Lytle, A. E. Fischer, C. P. Rhodes, T. M. McEvoy, M. E. Bourg and A. M. Lubers, *Chem. Soc. Rev.*, 2009, **38**, 226-252.
14. D. Koziej, A. Lauria and M. Niederberger, *Adv. Mater.*, 2014, **26**, 235-256.
15. S. Mahadik-Khanolkar, S. Donthula, A. Bang, C. Wisner, C. Sotiriou-Leventis and N. Leventis, *Chem. Mater.*, 2014, **26**, 1318-1331.
16. W. Zhang and W. Zheng, *Adv. Funct. Mater.*, 2016, **26**, 2988-2993.
17. C. Zhu, S. Fu, Q. Shi, D. Du and Y. Lin, *Angew. Chem. Int. Ed.*, 2017, **56**, 13944-13960.

18. Q. Zuo, T. Liu, C. Chen, Y. Ji, X. Gong, Y. Mai and Y. Zhou, *Angew. Chem. Int. Ed.*, 2019, **58**, 10198-10220
19. P. Zhou, F. Lv, N. Li, Y. Zhang, Z. Mu, Y. Tang, J. Lai, Y. Chao, M. Luo and F. Lin, *Nano energy*, 2019, **56**, 127-137.
20. L. Zhang, K. Doyle-Davis and X. Sun, *Energy Environ. Sci.*, 2019, **12**, 492-517.
21. J. Zhang, Y. Zhao, X. Guo, C. Chen, C.-L. Dong, R.-S. Liu, C.-P. Han, Y. Li, Y. Gogotsi and G. Wang, *Nat. Catal.*, 2018, **1**, 985.
22. H. Zhang, G. Liu, L. Shi and J. Ye, *Adv. Energy Mater.*, 2018, **8**, 1701343.
23. A. J. Therrien, A. J. Hensley, M. D. Marcinkowski, R. Zhang, F. R. Lucci, B. Coughlin, A. C. Schilling, J.-S. McEwen and E. C. H. Sykes, *Nat. Catal.*, 2018, **1**, 192.
24. Y. Peng, Z. Geng, S. Zhao, L. Wang, H. Li, X. Wang, X. Zheng, J. Zhu, Z. Li and R. Si, *Nano Lett.*, 2018, **18**, 3785-3791.
25. W. H. Lai, B. W. Zhang, Z. Hu, X. M. Qu, Y. X. Jiang, Y. X. Wang, J. Z. Wang, H. K. Liu and S. L. Chou, *Adv. Funct. Mater.*, 2019, 1807340.
26. J. Kim, C. W. Roh, S. K. Sahoo, S. Yang, J. Bae, J. W. Han and H. Lee, *Adv. Energy Mater.*, 2018, **8**, 1701476.
27. K. Jiang, B. Liu, M. Luo, S. Ning, M. Peng, Y. Zhao, Y.-R. Lu, T.-S. Chan, F. M. de Groot and Y. Tan, *Nat. Commun.*, 2019, **10**, 1743.
28. D. Huang, G. A. de Vera, C. Chu, Q. Zhu, E. Stavitski, J. Mao, H. Xin, J. A. Spies, C. A. Schmuttenmaer and J. Niu, *ACS Catal.*, 2018, **8**, 9353-9358.
29. X. Fang, Q. Shang, Y. Wang, L. Jiao, T. Yao, Y. Li, Q. Zhang, Y. Luo and H. L. Jiang, *Adv. Mater.*, 2018, **30**, 1705112.
30. Y. Chen, S. Ji, C. Chen, Q. Peng, D. Wang and Y. Li, *Joule*, 2018, **2**, 1242-1264.
31. S. Cao, H. Li, T. Tong, H. C. Chen, A. Yu, J. Yu and H. M. Chen, *Adv. Funct. Mater.*, 2018, **28**, 1802169.
32. S. Yang, J. Kim, Y. J. Tak, A. Soon and H. Lee, *Angew. Chem. Int. Ed.*, 2016, **55**, 2058-2062.
33. P. Yin, T. Yao, Y. Wu, L. Zheng, Y. Lin, W. Liu, H. Ju, J. Zhu, X. Hong, Z. Deng, G. Zhou, S. Wei and Y. Li, *Angew. Chem. Int. Ed.*, 2016, **55**, 10800-10805.
34. S. Liang, B. Qiao, X. Song, C. Hao, A. Wang, T. Zhang and Y. Shi, *Nano Energy*, 2017, **39**, 1-8.
35. P. Liu, Y. Zhao, R. Qin, S. Mo, G. Chen, L. Gu, D. M. Chevrier, P. Zhang, Q. Guo, D. Zang, B. Wu, G. Fu and N. Zheng, *Science*, 2016, **352**, 797-801.
36. X. Li, W. Bi, L. Zhang, S. Tao, W. Chu, Q. Zhang, Y. Luo, C. Wu and Y. Xie, *Adv. Mater.*, 2016, **28**, 2427-2431.
37. F. Dvorak, M. Farnesi Camellone, A. Tovt, N. D. Tran, F. R. Negreiros, M. Vorokhta, T. Skala, I. Matolinova, J. Myslivecek, V. Matolin and S. Fabris, *Nat. Commun.*, 2016, **7**, 10801.
38. X. Cui, K. Junge, X. Dai, C. Kreyenschulte, M. M. Pohl, S. Wohlrab, F. Shi, A. Bruckner and M. Beller, *ACS Cent. Sci.*, 2017, **3**, 580-585.
39. P. Hu, Z. Huang, Z. Amghouz, M. Makkee, F. Xu, F. Kapteijn, A. Dikhtiarenko, Y. Chen, X. Gu and X. Tang, *Angew. Chem. Int. Ed.*, 2014, **53**, 3418-3421.
40. B. Zhang, H. Asakura, J. Zhang, J. Zhang, S. De and N. Yan, *Angew. Chem. Int. Ed.*, 2016, **55**, 8319-8323.
41. Max J. Hülsey, Jiaguang Zhang and N. Yan, *Adv. Mater.*, 2018, **30**, 1802304.
42. D. Malko, A. Kucernak and T. Lopes, *Nat. Commun.*, 2016, **7**, 13285.
43. Z. Zhang, Y. Zhu, H. Asakura, B. Zhang, J. Zhang, M. Zhou, Y. Han, T. Tanaka, A. Wang, T. Zhang and N. Yan, *Nat. Commun.*, 2017, **8**, 16100.
44. C. H. Choi, M. Kim, H. C. Kwon, S. J. Cho, S. Yun, H. T. Kim, K. J. Mayrhofer, H. Kim and M. Choi, *Nat. Commun.* , 2016, **7**, 10922.45. C. Zhang, J. Sha, H. Fei, M. Liu, S. Yazdi, J. Zhang, Q. Zhong, X. Zou, N. Zhao, H. Yu, Z. Jiang, E. Ringe, B. I. Yakobson, J. Dong, D. Chen and J. M. Tour, *ACS Nano*, 2017, **11**, 6930-6941.
46. J. Deng, H. Li, J. Xiao, Y. Tu, D. Deng, H. Yang, H. Tian, J. Li, P. Ren and X. Bao, *Energy Environ. Sci.*, 2015, **8**, 1594-1601.
47. C. Zhu, S. Fu, J. Song, Q. Shi, D. Su, M. H. Engelhard, X. Li, D. Xiao, D. Li, L. Estevez, D. Du and Y. Lin, *Small*, 2017, **13**, 1603407.
48. F. Wang, A. Dong and W. E. Buhro, *Chem. Rev.*, 2016, **116**, 10888-10933.
49. J. Wang, K. Chen, M. Gong, B. Xu and Q. Yang, *Nano Lett.*, 2013, **13**, 3996-4000.
50. Y. Zhang, R. Xu, W. Chen, O. Zhuo, Q. Wu, J. Cai, X. Wang and Z. Hu, *J. Mater. Chem. C*, 2017, **5**, 6493-6496.
51. M. Amato, M. Palummo, R. Rurali and S. Ossicini, *Chem. Rev.*, 2014, **114**, 1371-1412.
52. X. Yang, B. Zhou, C. Liu, Y. Sui, G. Xiao, Y. Wei, X. Wang and B. Zou, *Nano Res.*, 2017, **10**, 2311-2320.
53. F. J. Heiligtag, W. Cheng, V. R. de Mendonça, M. J. Süess, K. Hametner, D. Günther, C. Ribeiro and M. Niederberger, *Chem. Mater.*, 2014, **26**, 5576-5584.
54. S. M. Jung, H. Y. Jung, M. S. Dresselhaus, Y. J. Jung and J. Kong, *Sci. Rep.*, 2012, **2**, 849.
55. W. Cheng, F. Rechberger and M. Niederberger, *Nanoscale*, 2016, **8**, 14074-14077.
56. Y. Tang, S. Gong, Y. Chen, L. W. Yap and W. Cheng, *ACS Nano*, 2014, **8**, 5707-5714.
57. H. L. Gao, L. Xu, F. Long, Z. Pan, Y. X. Du, Y. Lu, J. Ge and S. H. Yu, *Angew. Chem. Int. Ed.*, 2014, **53**, 4561-4566.
58. H. S. Yu, X. J. Wei, J. Li, S. Gu, S. Zhang, L. Wang, J. Y. Ma, L. n. Li, Q. Gao, R. Si, F. Sun, Y. Wang, F. Song, H. j. Xu, X. H. Yu, Y. Zou, J. q. Wang, Z. Jiang and Y. Y. Huang, *Nucl. Sci. Tech.*, 2015, **26**, 050102.
59. L. Wu, F. Xu, Y. Zhu, A. B. Brady, J. Huang, J. L. Durham, E. Dooryhee, A. C. Marschilok, E. S. Takeuchi and K. J. Takeuchi, *ACS Nano*, 2015, **9**, 8430-8439.
60. Z. Yang, D. C. Ford, J. S. Park, Y. Ren, S. Kim, H. Kim, T. T. Fister, M. K. Y. Chan and M. M. Thackeray, *Chem. Mater.*, 2017, **29**, 1507-1517.
61. S. Ni, H. Zhang, Y. Zhao, X. Li, Y. Sun, J. Qian, Q. Xu, P. Gao, D. Wu, K. Kato, M. Yamauchi and Y. Sun, *Chem. Eng. J.*, 2019, **366**, 631-638.
62. X. P. Li, J. Liu, Y. H. Zhao, H. J. Zhang, F. P. Du, C. Lin, T. J. Zhao and Y. H. Sun, *ChemCatChem*, 2015, **7**, 1848-1856.
63. Y. M. Dai, S. C. Tang, S. Vongehr and X. K. Meng, *ACS Sustain. Chem. Eng.*, 2014, **2**, 692-698.
64. Z. Li, Y. Ding, Y. Xiong and Y. Xie, *Cryst. Growth Des.*, 2005, **5**, 1953-1958.
65. G. Kresse and J. Furthmüller, *Comput. Mater. Sci.*, 1996, **6**, 15-50.
66. G. Kresse and J. Furthmüller, *Phys. Rev. B*, 1996, **54**, 11169-11186.
67. G. Kresse and J. Hafner, *Phys. Rev. B*, 1993, **47**, 558-561.
68. T. Sun, Y. Jiang, Q. Wu, L. Du, Z. Zhang, L. Yang, X. Wang and Z. Hu, *Catal. Sci. Technol.*, 2017, **7**, 51-55.
69. J. K. Nørskov, J. Rossmeisl, A. Logadottir, L. Lindqvist, J. R. Kitchin, T. Bligaard and H. Jónsson, *J. Phys. Chem. B*, 2004, **108**, 17886-17892.
70. Y. Jiang, L. Yang, T. Sun, J. Zhao, Z. Lyu, O. Zhuo, X. Wang, Q. Wu, J. Ma and Z. Hu, *ACS Catal.*, 2015, **5**, 6707-6712.
71. S. Kattel and G. Wang, *J. Phys. Chem. Lett.*, 2014, **5**, 452-456.

72. X. Liu, H. Liu, C. Chen, L. Zou, Y. Li, Q. Zhang, B. Yang, Z. Zou and H. Yang, *Nano Res.*, 2019, **12**, 1651-1657.

Title: Novel Self-Assembling Approach for Synthesizing Nanofiber Aerogel Supported Platinum Single Atoms

Haojie Zhang,[a,†] Yonghui Zhao,[b,†] Yu Sun,[c] Qing Xu,[b] Ruoou Yang,[d] Hao Zhang,[d] Chao Lin,[a] Kenich Kato,[e] Xiaopeng Li,[a,*] Miho Yamauchi[f,g,*] and Zheng Jiang[d,h,*]

TOC figure

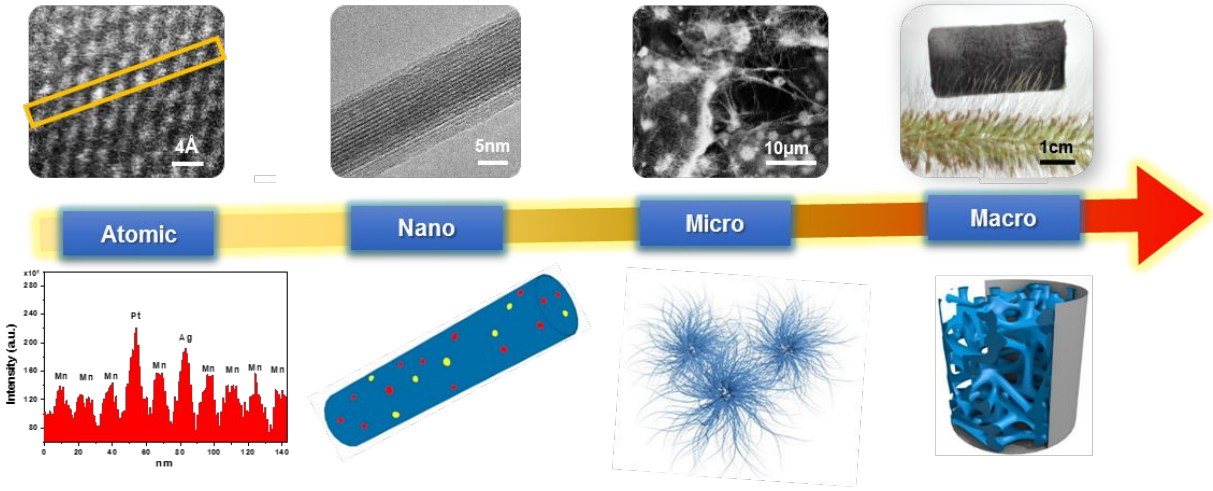

A new self-assembling methodology of incorporating Pt single atoms into metal oxide is presented with controlled structural formation over the entire range of length scales. Pt single atoms work synergistically with neighboring Mn atoms as asymmetrical sites for electrocatalytic reaction, resulting in activity enhancement.

Keywords: Platinum single atoms; Manganese oxide aerogel; Self-assembly; Solution-solid-solid (SSS) nanowire growth; Oxygen reduction reaction (ORR)